

# Bardeen spacetime as quantum corrected black hole: Grey-body factors and quasinormal modes of gravitational perturbations

Bekir Can Lütfüoğlu,<sup>1,\*</sup> Javlon Rayimbaev,<sup>2,3,4,†</sup> Sardor Murodov,<sup>5,6,‡</sup>  
Jakhongir Kurbanov,<sup>7,§</sup> and Muhammad Matyoqubov<sup>8,¶</sup>

<sup>1</sup>*Department of Physics, Faculty of Science, University of Hradec Králové,  
Rokitanského 62/26, 500 03 Hradec Králové, Czech Republic*

<sup>2</sup>*Tashkent International University of Education, Imom Bukhoriy 6, Tashkent 100207, Uzbekistan*

<sup>3</sup>*University of Tashkent for Applied Sciences, Gavhar Str. 1, Tashkent 700127, Uzbekistan*

<sup>4</sup>*Institute of Theoretical Physics, National University of Uzbekistan, Tashkent 100174, Uzbekistan*

<sup>5</sup>*New Uzbekistan University, Movarounnahr Str. 1, Tashkent 100000, Uzbekistan*

<sup>6</sup>*Tashkent State Technical University, Tashkent 100095, Uzbekistan*

<sup>7</sup>*Kimyo International University in Tashkent, Shota Rustaveli Street 156, Tashkent 100121, Uzbekistan*

<sup>8</sup>*Mamun University, Bolkhovuz Street 2, Khiva 220900, Uzbekistan*

We study axial gravitational perturbations of the asymptotically flat Bardeen spacetime interpreted as a string-T-duality-inspired quantum-corrected Schwarzschild black hole. Starting from the anisotropic-fluid background, we derive the Regge–Wheeler-type master equation and the corresponding effective potential, and compute quasinormal modes with high-order WKB–Padé and time-domain methods. We show that increasing the quantum-correction scale  $\ell_0$  raises and shifts the barrier inward, causing the black hole to ring at higher frequencies and decay more slowly. The same deformation suppresses low-frequency transmission, shifts the onset of grey-body factors to larger frequencies, and reorganizes the partial and total absorption cross-sections. Overall, the results identify a clear and consistent imprint of short-distance regularization on both ringdown and scattering observables.

## I. INTRODUCTION

The ringdown stage of a perturbed black hole is governed by a discrete set of complex frequencies known as quasinormal modes (QNMs), whose real and imaginary parts determine the oscillation frequency and damping time, respectively. Because these modes are fixed by the background geometry and by the spin of the perturbing field, they provide one of the cleanest probes of the near-horizon region and of possible deviations from the classical black hole paradigm. In the era of gravitational-wave astronomy, QNMs have therefore become central both to black-hole spectroscopy and to precision tests of strong gravity, since the observed ringdown signal is directly sensitive to the underlying effective potential that governs perturbations [1–4]. This makes the gravitational QNM spectrum especially valuable for quantum-corrected geometries, where even a small deformation of the potential barrier may leave the fundamental mode only slightly changed while substantially affecting overtones and damping rates [5].

Grey-body factors (GBFs) provide complementary information. Hawking radiation is created near the event horizon, but the flux measured by an asymptotic observer is filtered by the curvature-induced potential barrier surrounding the black hole [6–8]. As a result, the emitted

spectrum is not exactly Planckian; rather, it is weighted by transmission coefficients that depend on frequency, angular momentum, and field spin [9]. GBFs therefore govern absorption probabilities, scattering amplitudes, and Hawking energy-emission rates, and they furnish a natural bridge between black-hole thermodynamics and wave propagation. Since QNMs and GBFs are determined by the same effective potential, albeit with different boundary conditions, studying both quantities together yields a considerably more complete characterization of a black hole than either observable alone [10–12].

Regular black holes are particularly attractive laboratories for such studies. They offer a phenomenological route toward resolving the spacetime singularity problem while preserving horizons and much of the familiar black-hole exterior. The Bardeen solution occupies a distinguished place in this program as the first regular black-hole geometry proposed in the literature [13]. It was later shown that the Bardeen metric can be supported by nonlinear electrodynamics, thereby endowing the model with a concrete matter source and a consistent dynamical interpretation [14, 15]. Since then, regular spacetimes have been used extensively to investigate how singularity resolution may affect stability, quasinormal spectra, shadows, lensing, thermodynamics, and Hawking radiation [16–54].

An especially appealing twist was proposed by Nicolini, Spallucci, and Wondrak, who showed that a neutral, regular black-hole solution obtained from a string-T-duality-inspired zero-point-length modification of the static potential is formally equivalent to the Bardeen geometry, up to the precise interpretation of the ultraviolet regulator [55]. In this picture, the Bardeen spacetime

\* bekir.lutfuoglu@uhk.cz

† javlon@astrin.uz

‡ mursardor@ifar.uz

§ jaxongir0903@gmail.com

¶ m\_matyoqubov@mamunedu.uz

can be read not merely as a nonlinear electrodynamics black hole, but also as an effective quantum-corrected Schwarzschild solution. This reinterpretation is important for phenomenology: it turns the Bardeen parameter into an economical proxy for short-distance quantum effects and provides a simple, regular geometry in which one can ask how quantum corrections modify classical observables without giving up analytic control over the background.

The perturbative properties of this spacetime have already attracted considerable attention, but mainly in the test-field sector. In particular, Konoplya, Ovchinnikov, and Ahmedov revisited the Bardeen spacetime in its quantum-corrected interpretation and computed accurate scalar, electromagnetic, and Dirac QNMs, together with GBFs and Hawking emission rates [10]. Their analysis showed that near-horizon quantum corrections can produce a pronounced outburst of overtones even when the fundamental mode stays close to its Schwarzschild counterpart, and that the same corrections substantially suppress Hawking radiation. Soon afterwards, Bolokhov investigated massive scalar perturbations of the same background and found quasinormal resonances, long-lived modes, and oscillatory late-time tails [56]. In parallel, related Bardeen-family geometries were studied in several settings: gravitational perturbations of the Bardeen black hole surrounded by quintessence were analyzed in Ref. [57]; electromagnetic and gravitational QNMs together with GBFs were investigated for the Bardeen-de Sitter spacetime in Ref. [19]; and the axial/polar gravitational sectors and their isospectrality properties were studied for Bardeen (anti-)de Sitter black holes in Ref. [20]. More broadly, recent work on quantum-corrected or regular black holes has reinforced the idea that short-distance modifications may leave robust signatures in higher overtones, absorption spectra, and the interplay between QNMs and GBFs [11, 12, 58–60].

Despite this progress, a dedicated study of gravitational QNMs and GBFs for the asymptotically flat Bardeen spacetime in the specific string-T-duality-inspired quantum-corrected interpretation is still missing. This gap is especially noteworthy because the gravitational sector is the most directly relevant one for black-hole spectroscopy: it determines the ringdown signal itself and controls the spin-2 transmission probabilities associated with graviton scattering and Hawking emission. The purpose of the present work is to fill this gap by deriving the gravitational perturbation equations for this background and by analyzing the corresponding QNM spectrum and grey-body factors. In this way, one can disentangle which signatures arise generically from regularity and which are genuinely tied to the quantum-corrected interpretation of the Bardeen geometry.

The remainder of this paper is organized as follows. In Sec. II we review the quantum-corrected Bardeen geometry and summarize its basic horizon and regularity properties. In Sec. III we derive the master equation and the corresponding axial effective potential for gravita-

tional perturbations. The WKB and time-domain methods used in the analysis are outlined in Secs. IV and V, respectively. Section VI presents the gravitational quasinormal spectra and their time-domain interpretation, while Sec. VII discusses the GBFs together with the partial and total absorption cross-sections (ACSs). Finally, Sec. VIII summarizes the main results and their physical implications.

## II. QUANTUM-CORRECTED BARDEEN SPACETIME

In the interpretation advocated by Nicolini, Spallucci, and Wondrak, the geometry under consideration is not viewed as a magnetic monopole solution of nonlinear electrodynamics, but rather as an effective neutral black-hole metric emerging from string T-duality through its connection with path-integral self-duality and the associated zero-point length of spacetime [55, 61]. In this picture, the short-distance structure of the propagator is modified in a nonperturbative way, so that the static Newtonian potential becomes regular instead of diverging at the origin. When this regularized source is coupled to gravity in the static, spherically-symmetric sector, one obtains a metric that is formally equivalent to the Bardeen spacetime [13, 15], but whose deformation parameter is reinterpreted as a quantum-correction scale rather than as a magnetic charge [10, 55].

Accordingly, throughout this work we consider the line element

$$ds^2 = -f(r)dt^2 + \frac{dr^2}{f(r)} + r^2(d\theta^2 + \sin^2\theta d\phi^2), \quad (1)$$

with metric function

$$f(r) = 1 - \frac{2Mr^2}{(r^2 + \ell_0^2)^{3/2}}, \quad (2)$$

where  $M$  is the asymptotic mass and  $\ell_0$  denotes the zero-point-length parameter induced by the underlying T-duality scenario. Following Ref. [55], one may relate this parameter to the Regge slope by  $\ell_0 = 2\pi\sqrt{\alpha'}$ , so that  $\ell_0$  is expected to be of the order of the Planck length. Since the geometry depends only on  $\ell_0^2$ , it is sufficient to restrict attention to  $\ell_0 \geq 0$ .

The basic properties of the metric are immediate from its asymptotic expansions. At large radial distance one finds

$$f(r) = 1 - \frac{2M}{r} + \frac{3M\ell_0^2}{r^3} + \mathcal{O}(r^{-5}), \quad (3)$$

which shows that the spacetime is asymptotically Schwarzschild, with the leading quantum correction entering only at order  $r^{-3}$ . By contrast, close to the center,

$$f(r) = 1 - \frac{2M}{\ell_0^3}r^2 + \mathcal{O}(r^4) = 1 - \frac{\Lambda_{\text{eff}}}{3}r^2 + \mathcal{O}(r^4), \quad (4)$$

where

$$\Lambda_{\text{eff}} = \frac{6M}{\ell_0^3}. \quad (5)$$

Therefore the Schwarzschild singularity is replaced by a de Sitter core, which is the key manifestation of regularity in this geometry [10, 55].

The horizons are determined by the roots of  $f(r) = 0$ . If  $r_+$  denotes the outer event horizon, then the horizon condition can be written as

$$M = \frac{(r_+^2 + \ell_0^2)^{3/2}}{2r_+^2}, \quad (6)$$

which is often convenient when one wishes to use the horizon radius rather than  $M$  as the fundamental scale [10]. For fixed positive mass, the black-hole sector exists only in the range

$$0 \leq \frac{\ell_0}{M} \leq \frac{4}{3\sqrt{3}}. \quad (7)$$

The lower endpoint reproduces the Schwarzschild geometry, while the upper endpoint corresponds to the extremal configuration where the inner and outer horizons merge. In that case,

$$\ell_0^{\text{ext}} = \frac{4M}{3\sqrt{3}}, \quad r_{\text{ext}} = \sqrt{2}\ell_0^{\text{ext}} = \sqrt{\frac{32}{27}}M. \quad (8)$$

For  $\ell_0/M > 4/(3\sqrt{3})$ , the spacetime remains everywhere regular but no longer possesses an event horizon. If instead one normalizes all quantities by  $r_+$ , then Eq. (6) implies the equivalent black-hole range

$$0 \leq \frac{\ell_0}{r_+} \leq \frac{1}{\sqrt{2}}. \quad (9)$$

In what follows, we shall be interested exclusively in the black-hole branch, namely in configurations with  $M > 0$  and parameter values satisfying Eq. (7). In this sector, increasing  $\ell_0$  strengthens the deviation from Schwarzschild predominantly in the near-horizon and interior regions, while leaving the far-zone geometry only weakly modified. This feature makes the metric especially suitable for the present analysis of gravitational QNMs and GBFs, since both observables are controlled by the effective scattering potential in precisely those regions where the quantum correction is most pronounced.

### III. AXIAL GRAVITATIONAL PERTURBATIONS

For the Nicolini interpretation of the Bardeen spacetime, the background is not vacuum: the geometry of Sec. II corresponds to an effective anisotropic fluid with nonvanishing density,

$$T^\mu{}_\nu = \text{diag}(-\rho_{\text{eff}}, p_{r,\text{eff}}, p_{t,\text{eff}}, p_{t,\text{eff}}), \quad (10)$$

These quantities are not written explicitly in Ref. [55]. Rather, they are reconstructed *a posteriori* by asking which effective energy-momentum tensor would reproduce the metric (2) through Einstein's equations. For a static line element (1) one has

$$\begin{aligned} 8\pi\rho_{\text{eff}}(r) &= \frac{1 - f(r) - rf'(r)}{r^2}, \\ 8\pi p_{r,\text{eff}}(r) &= \frac{-1 + f(r) + rf'(r)}{r^2} = -8\pi\rho_{\text{eff}}(r), \\ 8\pi p_{t,\text{eff}}(r) &= \frac{rf''(r) + 2f'(r)}{2r}. \end{aligned}$$

Substituting Eq. (2) into these relations gives precisely the effective density and pressures used below, namely

$$\rho_{\text{eff}}(r) = \frac{3M\ell_0^2}{4\pi(r^2 + \ell_0^2)^{5/2}}, \quad (11)$$

$$p_{r,\text{eff}}(r) = -\rho_{\text{eff}}(r), \quad (12)$$

$$p_{t,\text{eff}}(r) = \frac{3M\ell_0^2(3r^2 - 2\ell_0^2)}{8\pi(r^2 + \ell_0^2)^{7/2}}. \quad (13)$$

These are therefore effective source functions associated with the geometry, not additional matter fields postulated independently of the Nicolini construction. This point is important for the perturbation problem. As emphasized in the recent analysis of compact objects supported by anisotropic matter, different prescriptions for the matter sector can lead to inequivalent odd-parity spectra, so the treatment of gravitational perturbations must be stated explicitly rather than inferred from the metric alone [62]. In what follows we therefore formulate the axial problem in the effective Einstein description with the above nonzero density and pressures kept throughout the derivation.

We adopt the Regge–Wheeler gauge and expand the odd-parity metric perturbations in axial vector harmonics [63]. For each multipole  $(\ell, m)$  with  $\ell \geq 2$ , the nonvanishing components are

$$h_{aB}^{(-)} = \sum_{\ell m} h_a^{\ell m}(t, r) S_B^{\ell m}, \quad (14)$$

$$h_{ab}^{(-)} = 0, \quad h_{AB}^{(-)} = 0, \quad (15)$$

where  $a, b \in \{t, r\}$ ,  $A, B \in \{\theta, \phi\}$ , and

$$S_A^{\ell m} = \left( -\frac{1}{\sin\theta} \partial_\phi Y_{\ell m}, \sin\theta \partial_\theta Y_{\ell m} \right) \quad (16)$$

are the odd-parity vector spherical harmonics. Since  $\rho_{\text{eff}}$ ,  $p_{r,\text{eff}}$ , and  $p_{t,\text{eff}}$  are scalars on the two-sphere, they have no axial perturbations. The only odd-parity matter degree of freedom is the angular part of the fluid velocity, which we denote by

$$\delta u_A = U^{\ell m}(t, r) S_A^{\ell m}. \quad (17)$$

The perturbed conservation law for the effective stress tensor implies that this axial fluid variable is time independent. Therefore, for the QNM problem with harmonic dependence  $e^{-i\omega t}$  and  $\omega \neq 0$ , it can be consistently

set to zero. In this sense the odd-parity sector reduces to a single master field, but the background density and radial pressure still enter nontrivially through the linearized Einstein equations.

To derive the master equation it is useful to introduce the mass function

$$m(r) = \frac{Mr^3}{(r^2 + \ell_0^2)^{3/2}}, \quad f(r) = 1 - \frac{2m(r)}{r}, \quad (18)$$

so that the background Einstein equations give

$$m'(r) = 4\pi r^2 \rho_{\text{eff}}(r). \quad (19)$$

After substituting the odd-parity ansatz into the  $tB$  and  $rB$  components of the linearized Einstein equations, eliminating  $h_0$  in favor of  $h_1$ , and using the background equations to remove derivatives of the metric, one obtains for each multipole a Regge–Wheeler-type equation for

$$\Psi(r) = \frac{f(r)}{r} h_1(r) \quad (20)$$

in terms of the tortoise coordinate

$$\frac{dr_*}{dr} = \frac{1}{f(r)}. \quad (21)$$

The master equation takes the form

$$\frac{d^2 \Psi}{dr_*^2} + [\omega^2 - V_{\text{ax}}(r)] \Psi = 0, \quad (22)$$

with effective potential

$$V_{\text{ax}}(r) = f(r) \left[ \frac{\ell(\ell+1)}{r^2} - \frac{6m(r)}{r^3} + 4\pi(\rho_{\text{eff}}(r) - p_{r,\text{eff}}(r)) \right]. \quad (23)$$

Equation (23) is the form appropriate to an anisotropic effective fluid with nonzero density, matching the odd-parity master potential used for static spherically symmetric anisotropic-fluid backgrounds in Ref. [62]; see also Ref. [64] for the corresponding dirty-black-hole Regge–Wheeler framework. This is the point at which our derivation differs conceptually from a purely geometric treatment.

For the quantum-corrected Bardeen background the effective equation of state is special, because  $p_{r,\text{eff}} = -\rho_{\text{eff}}$ . Hence

$$V_{\text{ax}}(r) = f(r) \left[ \frac{\ell(\ell+1)}{r^2} - \frac{6m(r)}{r^3} + 8\pi\rho_{\text{eff}}(r) \right]. \quad (24)$$

Substituting Eqs. (19) and the explicit expressions for  $m(r)$  and  $\rho_{\text{eff}}(r)$ , we obtain

$$V_{\text{ax}}(r) = f(r) \left[ \frac{\ell(\ell+1)}{r^2} - \frac{6M}{(r^2 + \ell_0^2)^{3/2}} + \frac{6M\ell_0^2}{(r^2 + \ell_0^2)^{5/2}} \right] \quad (25)$$

$$= f(r) \left[ \frac{\ell(\ell+1)}{r^2} - \frac{6Mr^2}{(r^2 + \ell_0^2)^{5/2}} \right]. \quad (26)$$

Thus, for this particular background, the explicit density term combines with the mass-function term into the compact potential (26). This simplification is a consequence of the specific relation  $p_{r,\text{eff}} = -\rho_{\text{eff}}$  and should not be interpreted as a general equivalence between different prescriptions for matter perturbations.

The resulting potential has the expected limits. At the event horizon,  $f(r_+) = 0$ , so  $V_{\text{ax}}(r_+) = 0$ . In the Schwarzschild limit,  $\ell_0 \rightarrow 0$ , Eq. (26) reduces to the standard Regge–Wheeler barrier,

$$V_{\text{RW}}(r) = \left( 1 - \frac{2M}{r} \right) \left[ \frac{\ell(\ell+1)}{r^2} - \frac{6M}{r^3} \right]. \quad (27)$$

At large  $r$  one has

$$V_{\text{ax}}(r) = \frac{\ell(\ell+1)}{r^2} - \frac{2M[\ell(\ell+1)+3]}{r^3} + \mathcal{O}(r^{-4}), \quad (28)$$

so the asymptotic solutions of Eq. (22) are plane waves,  $\Psi \sim e^{\pm i\omega r_*}$ , and the usual QNM and scattering boundary conditions apply.

We emphasize that Eq. (26) is the axial potential that follows from the nonvacuum, anisotropic-fluid interpretation of the Nicolini geometry. In the subsequent sections this is the potential we use for both the QNM calculation and the GBF analysis.

Representative profiles of the potential (26) are shown in Fig. 1 for  $M = 1$  and for the same values  $\ell_0 = 0.01, 0.5,$  and  $0.769$  that will later be used in the scattering analysis. For fixed  $\ell$ , increasing  $\ell_0$  raises the barrier and shifts its maximum toward smaller  $r/M$ , while increasing  $\ell$  produces the expected centrifugal enhancement of the barrier. These trends already indicate that larger  $\ell$  and larger  $\ell_0$  should postpone the onset of transmission and move the relevant scattering and absorption structures to higher frequencies.

#### IV. WKB METHOD

To compute the quasinormal frequencies we employ the standard WKB treatment of barrier-penetration problems for black-hole perturbations. The first-order version was introduced by Schutz and Will [65], then extended to third order by Iyer and Will [66], and later pushed to sixth order by Konoplya [67]. In its modern implementation, the method is further improved by Padé resummation of the high-order WKB series, following the strategy advocated by Matyjasek and Opala [68]. This is the approach adopted in the present work.

For the axial master equation (22) it is convenient to write

$$\frac{d^2 \Psi}{dr_*^2} + Q(r_*) \Psi = 0, \quad Q(r_*) \equiv \omega^2 - V_{\text{ax}}(r). \quad (29)$$

Quasinormal modes are defined by the boundary conditions of a purely ingoing wave at the event horizon and

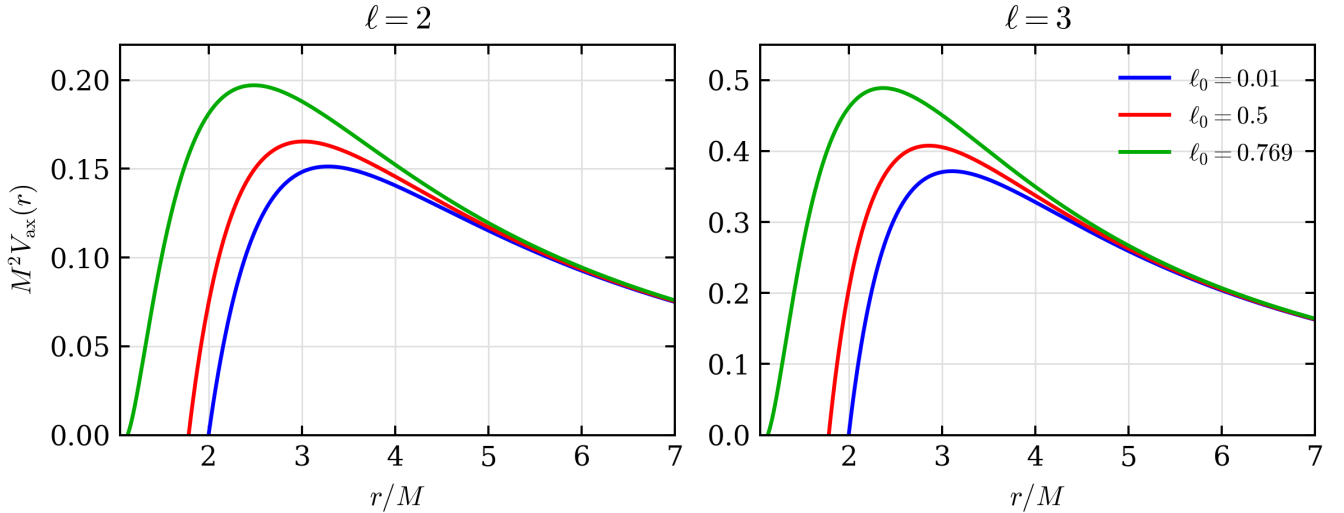


FIG. 1. Representative axial effective potentials  $M^2 V_{\text{ax}}(r)$  as functions of  $r/M$  for the quantum-corrected Bardeen black hole with  $M = 1$ . Panel (a) corresponds to  $\ell = 2$  and panel (b) to  $\ell = 3$ . In each panel, the blue, red, and green curves denote  $\ell_0 = 0.01, 0.5$ , and  $0.769$ , respectively.

a purely outgoing wave at spatial infinity,

$$\Psi \sim \begin{cases} e^{-i\omega r_*}, & r_* \rightarrow -\infty, \\ e^{+i\omega r_*}, & r_* \rightarrow +\infty. \end{cases} \quad (30)$$

The WKB construction applies when the effective potential forms a smooth, single-peaked barrier. For the black-hole branch considered here and for the low-lying modes studied below, the axial potential satisfies precisely this condition.

Let  $r_{*0}$  denote the position of the maximum of the barrier, so that  $Q_0 \equiv Q(r_{*0})$  and  $Q_0^{(p)} \equiv d^p Q/dr_*^p|_{r_{*0}}$ . Expanding  $Q(r_*)$  in a Taylor series about  $r_{*0}$ , matching the WKB solutions across the turning points, and imposing the quasinormal boundary conditions yield the usual WKB quantization condition

$$\frac{iQ_0}{\sqrt{2Q_0^{(2)}}} - \sum_{k=2}^N \Lambda_k = n + \frac{1}{2}, \quad (31)$$

where  $n = 0, 1, 2, \dots$  is the overtone number and the quantities  $\Lambda_k$  are higher-order correction terms built from the derivatives of  $Q$  at the peak. At first order one keeps only the leading term in Eq. (31), the Iyer–Will extension incorporates the second- and third-order corrections  $\Lambda_2$  and  $\Lambda_3$ , and the Konoplya formula includes all corrections up to  $\Lambda_6$  [65–67]. In general, an  $N$ th-order WKB formula involves peak derivatives up to  $Q_0^{(2N)}$ ; thus the 14th- and 16th-order calculations quoted in our tables require derivatives of  $Q$  up to the 28th and 32nd orders, respectively.

For the present Bardeen background the effective potential is frequency independent, so the WKB procedure can be implemented directly. We first locate the

peak  $r_0$  of  $V_{\text{ax}}(r)$  outside the event horizon by solving  $dV_{\text{ax}}/dr = 0$ . Since  $dr_*/dr = 1/f(r)$  and  $f(r) > 0$  for  $r > r_+$ , the maxima in the coordinates  $r$  and  $r_*$  coincide. The derivatives with respect to the tortoise coordinate are then obtained from  $d/dr_* = f(r)d/dr$  and evaluated at  $r = r_0$ . Equation (31) is subsequently solved numerically for each pair  $(\ell, n)$ , and the physically relevant branch is selected by the damping condition  $\text{Im}(\omega) < 0$ .

A substantial improvement in accuracy is obtained by treating the WKB result as a formal asymptotic series for  $\omega^2$  and resumming it by a Padé approximant rather than using the truncated polynomial directly [68]. Introducing an auxiliary bookkeeping parameter  $\epsilon$ , one writes

$$\omega^2(\epsilon) = V_0 - i\mathcal{K}\sqrt{2Q_0^{(2)}}\epsilon - i\sqrt{2Q_0^{(2)}}\sum_{k=2}^N \epsilon^k \Lambda_k, \quad (32)$$

$$\mathcal{K} = n + \frac{1}{2},$$

with  $V_0 \equiv V_{\text{ax}}(r_0)$ , and only at the end sets  $\epsilon = 1$ . One then constructs the rational function

$$P_n^{\tilde{m}}(\epsilon) = \frac{\sum_{j=0}^{\tilde{n}} A_j \epsilon^j}{1 + \sum_{j=1}^{\tilde{m}} B_j \epsilon^j}, \quad (33)$$

whose Taylor expansion reproduces Eq. (32) through the chosen order. In the present work we use diagonal Padé approximants. Therefore, the notation WKB14 ( $\tilde{m} = 7$ ) in the tables means that the 14th-order WKB series for  $\omega^2$  has been resummed by the diagonal Padé approximant  $P_7^7(\epsilon)$ , while WKB16 ( $\tilde{m} = 8$ ) denotes the 16th-order series resummed by  $P_8^8(\epsilon)$ . The agreement between these two high-order, diagonal Padé estimates provides an internal consistency check on the quoted quasinormal frequencies.

As in the standard literature, the WKB method is most reliable for smooth, single-barrier potentials and for low overtones, typically when  $n < \ell$  or, more cautiously, when  $n$  is not too close to the top of the available angular spectrum [67, 68]. Its accuracy improves with increasing  $\ell$  and generally deteriorates for large overtones, for broad or non-single-peaked barriers, and near situations in which the turning-point picture becomes marginal [69–95]. For this reason we use the method below primarily for the fundamental mode and the first few overtones, precisely the regime in which it is known to give the most accurate black-hole quasinormal frequencies.

## V. TIME-DOMAIN INTEGRATION METHOD

Although the numerical values quoted below are obtained with the WKB–Padé approach, it is useful to summarize the standard time-domain evolution scheme that is commonly used to extract the ringdown signal directly from the master equation and to monitor the transition from quasinormal ringing to late-time tails. Introducing the null coordinates

$$u = t - r_*, \quad v = t + r_*, \quad (34)$$

the time-dependent version of Eq. (22) becomes

$$4 \frac{\partial^2 \Psi}{\partial u \partial v} + V_{\text{ax}}(r(u, v)) \Psi = 0. \quad (35)$$

For black-hole perturbations, a convenient characteristic discretization of this equation was employed by Gundlach, Price, and Pullin in their analysis of quasinormal ringing and late-time tails [96]. If  $S = (u, v)$ ,  $E = (u, v + \Delta)$ ,  $W = (u + \Delta, v)$ , and  $N = (u + \Delta, v + \Delta)$  denote the corners of a null grid cell, then the field update is

$$\Psi_N = \Psi_W + \Psi_E - \Psi_S - \frac{\Delta^2}{8} V_{\text{ax}}(S)(\Psi_W + \Psi_E) + \mathcal{O}(\Delta^4). \quad (36)$$

One usually specifies a Gaussian pulse on one initial null ray and trivial data on the other, then records the waveform at fixed  $r_*$  as a function of the time coordinate  $t = (u + v)/2$ .

The quasinormal part of the signal can then be fitted by a superposition of damped exponentials. For equally spaced samples  $x_n \equiv \Psi(t_0 + n\Delta t)$ , the classical Prony procedure [97] assumes the representation

$$x_n = \sum_{j=1}^p C_j z_j^n, \quad z_j = e^{-i\omega_j \Delta t}, \quad (37)$$

so that the complex frequencies follow from the roots  $z_j$  of the associated linear-prediction polynomial via

$$\omega_j = \frac{i}{\Delta t} \ln z_j. \quad (38)$$

This provides a direct way to extract the dominant quasinormal frequencies from the numerically evolved waveform once the initial transient has passed and before the power-law tail takes over. The time-domain integration has been effectively used in numerous works for testing stability and detecting dominant QNMs [98–119]. For a broad review of time-domain evolution, late-time tails, and other numerical as well as semianalytical methods used in black-hole perturbation theory, see Ref. [120].

## VI. GRAVITATIONAL QUASINORMAL MODES

The quasinormal spectra collected in Tables I–III show a clear and systematic dependence on the quantum-correction parameter  $\ell_0$ . For every mode listed, increasing  $\ell_0$  shifts the spectrum toward larger oscillation frequencies and weaker damping, i.e.,  $Re(\omega)$  increases while  $|Im(\omega)|$  decreases. For the fundamental  $\ell = 2$  mode, for example,  $\omega$  changes from  $0.374370 - 0.088885i$  at  $\ell_0 = 0.1$  to  $0.432944 - 0.071693i$  at  $\ell_0 = 0.769$ , whereas for the fundamental  $\ell = 3$  mode it changes from  $0.600497 - 0.092602i$  to  $0.691612 - 0.075187i$  over the same interval. The same qualitative trend is seen for the first few overtones: at fixed  $\ell$ , higher overtones remain more damped than the fundamental mode, but increasing  $\ell_0$  still moves them upward in  $Re(\omega)$  and closer to the real axis. Thus the quantum-corrected Bardeen black hole rings both faster and longer than its near-Schwarzschild counterpart.

The multipole dependence is summarized in Table IV, where the fundamental mode is displayed for fixed  $\ell_0 = 0.769$ . As  $\ell$  increases from 2 to 20, the real part of the frequency grows from 0.432944 to 4.515921, while the damping rate varies only mildly, from 0.071693 to 0.077940. Therefore the real part grows almost linearly with  $\ell$ , whereas  $|Im(\omega)|$  rapidly approaches an approximately constant value. This is the expected eikonal behavior: higher multipoles oscillate much more rapidly, but their damping time changes comparatively little.

This trend can be made quantitative in the eikonal regime. For large  $L \equiv \ell + 1/2$ , the axial potential (26) takes the form

$$V_{\text{ax}}(r) = L^2 \frac{f(r)}{r^2} + \mathcal{O}(L^0). \quad (39)$$

Hence the peak of the leading barrier is determined by

$$\left. \frac{d}{dr} \left( \frac{f(r)}{r^2} \right) \right|_{r=r_{\text{ph}}} = 0 \quad \iff \quad 2f(r_{\text{ph}}) = r_{\text{ph}} f'(r_{\text{ph}}), \quad (40)$$

that is, by the outer unstable null orbit. For the Bardeen metric (2), this condition becomes

$$3Mr_{\text{ph}}^4 = (r_{\text{ph}}^2 + \ell_0^2)^{5/2}. \quad (41)$$

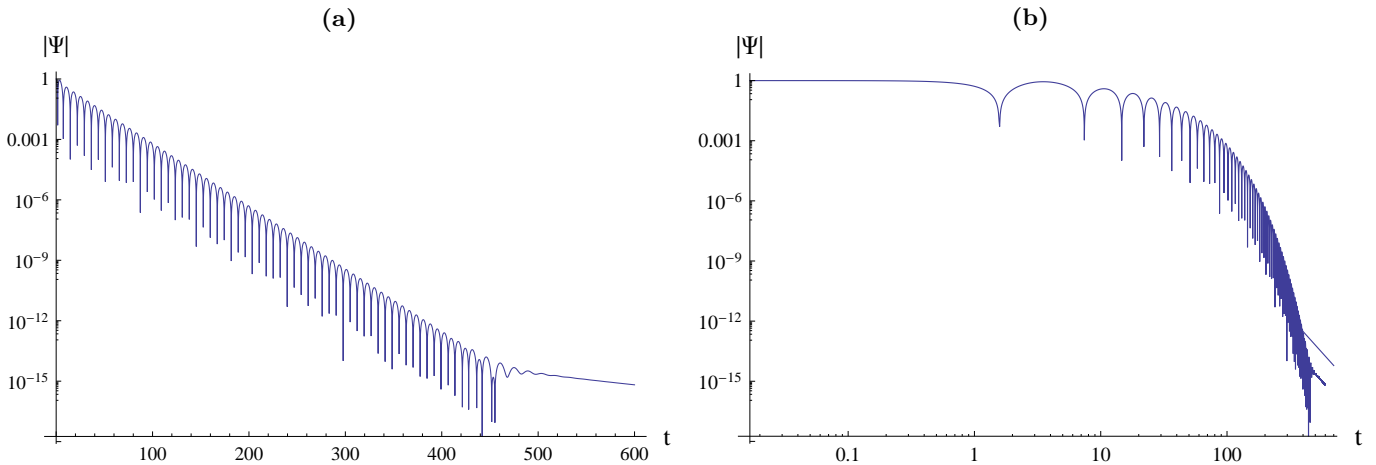


FIG. 2. Time-domain profile of the axial gravitational perturbation for the Bardeen black hole with  $\ell = 2$ ,  $\ell_0 = 0.769$ , and  $M = 1$ . Panel (a) shows the semilogarithmic profile of  $|\Psi|$ , displaying the quasinormal ringing and the onset of the late-time tail. Panel (b) shows the same signal on log-log axes, where the asymptotic decay  $|\Psi| \propto t^{-7}$  is visible. The fundamental frequency extracted by the Prony method coincides with the WKB–Padé value for the same parameters.

Keeping only the leading term in the WKB formula (31) and expanding in inverse powers of  $L$ , one finds the gravitational counterpart of the test-field eikonal formula discussed in Ref. [10],

$$\omega_{\ell n} = L \Omega_c - i \left( n + \frac{1}{2} \right) \lambda_c + \mathcal{O}(L^{-1}),$$

$$L \equiv \ell + \frac{1}{2},$$
(42)

where

$$\Omega_c^2 = \frac{f(r_{\text{ph}})}{r_{\text{ph}}^2} = \frac{r_{\text{ph}}^2 - 2\ell_0^2}{3r_{\text{ph}}^4},$$
(43)

$$\lambda_c^2 = \frac{(r_{\text{ph}}^2 - 4\ell_0^2)(r_{\text{ph}}^2 - 2\ell_0^2)}{3r_{\text{ph}}^4(r_{\text{ph}}^2 + \ell_0^2)}$$
(44)

$$= \frac{f(r_{\text{ph}})}{2r_{\text{ph}}^2} [2f(r_{\text{ph}}) - r_{\text{ph}}^2 f''(r_{\text{ph}})].$$
(45)

For the fixed value  $\ell_0 = 0.769$  used in Table IV, the outer solution of Eq. (41) is  $r_{\text{ph}} \simeq 2.30360 M$ , which gives  $\Omega_c M \simeq 0.220941$  and  $\lambda_c M \simeq 0.156021$ . Therefore, for the fundamental mode,

$$\omega_{\ell 0} M \simeq 0.220941 \left( \ell + \frac{1}{2} \right) - 0.078011 i.$$
(46)

Comparison with Table IV shows that the eikonal formula converges monotonically from above. In the real part, the deviation decreases from 4.35% at  $\ell = 5$  to 1.14% at  $\ell = 10$  and 0.30% at  $\ell = 20$ ; for  $|Im(\omega)|$ , the corresponding deviations are 1.36%, 0.35%, and 0.09%. Thus the table confirms the analytic eikonal law very well once  $\ell \gtrsim 10$ : the damping rate is already in the sub-percent regime for moderate multipoles, while the oscillation frequency approaches the same level slightly more slowly.

The internal accuracy of the semianalytic calculation can be assessed from the comparison between the 16th- and 14th-order WKB–Padé approximants. For the fundamental mode the agreement is excellent: the discrepancy never exceeds 0.0142% for  $\ell = 2$  and is zero at the displayed precision for  $\ell = 3$ . For the first overtone the maximal mismatch is still only 0.0634% for  $\ell = 2$  and  $2 \times 10^{-5}\%$  for  $\ell = 3$ . The higher overtones behave as expected from the usual WKB domain of validity: the agreement remains very good for the  $\ell = 3$  spectrum, while the largest deviation in the whole data set is 1.53% for the  $\ell = 2$ ,  $n = 2$ ,  $\ell_0 = 0.5$  mode, where the condition  $n < \ell$  is only marginally satisfied. Independent support comes from the time-domain profile shown in Fig. 2: the Prony extraction of the fundamental mode for  $\ell = 2$  and  $\ell_0 = 0.769$  reproduces the same frequency  $\omega = 0.432944 - 0.071693 i$  as the WKB–Padé calculation.

A convenient measure of how good an oscillator the black hole is is the quality factor,

$$Q_{\ell n} \equiv \frac{Re(\omega)_{\ell n}}{2|Im(\omega)_{\ell n}|}.$$
(47)

Larger  $Q_{\ell n}$  means that the system performs more oscillations before the signal is substantially damped. For the fundamental  $\ell = 2$  mode, Fig. 3 shows that  $Q$  grows monotonically with the quantum-correction parameter, from  $Q \simeq 2.106$  at  $\ell_0 = 0.1$  to  $Q \simeq 3.019$  at  $\ell_0 = 0.769$ . Since the classical Schwarzschild black hole is recovered in the limit  $\ell_0 \rightarrow 0$ , this monotonic increase implies that within this family the quantum-corrected black holes are better oscillators than the classical one, and the near-extremal configurations are the best oscillators of all.

The time-domain evolution confirms the same picture. After the initial burst, the signal first enters the ringdown regime,

$$\Psi(t, r_*) \approx A e^{-i\omega_0 t},$$
(48)

$\ell_0$	WKB16 ( $\tilde{m} = 8$ )	WKB14 ( $\tilde{m} = 7$ )	Difference
$\ell = 2, n = 0$			
0.1	0.374370 - 0.088885 <i>i</i>	0.374360 - 0.088869 <i>i</i>	0.0047%
0.15	0.375275 - 0.088706 <i>i</i>	0.375232 - 0.088740 <i>i</i>	0.0142%
0.2	0.376476 - 0.088543 <i>i</i>	0.376471 - 0.088551 <i>i</i>	0.00254%
0.25	0.378099 - 0.088296 <i>i</i>	0.378097 - 0.088298 <i>i</i>	0.0008%
0.3	0.380135 - 0.087969 <i>i</i>	0.380135 - 0.087969 <i>i</i>	0.0001%
0.35	0.382616 - 0.087551 <i>i</i>	0.382616 - 0.087551 <i>i</i>	0%
0.4	0.385589 - 0.087021 <i>i</i>	0.385589 - 0.087021 <i>i</i>	0.00005%
0.45	0.389111 - 0.086351 <i>i</i>	0.389111 - 0.086351 <i>i</i>	$0. \times 10^{-4}$ %
0.5	0.393261 - 0.085497 <i>i</i>	0.393261 - 0.085497 <i>i</i>	0%
0.55	0.398144 - 0.084395 <i>i</i>	0.398144 - 0.084395 <i>i</i>	0.00002%
0.6	0.403901 - 0.082946 <i>i</i>	0.403902 - 0.082946 <i>i</i>	0.0001%
0.65	0.410728 - 0.080978 <i>i</i>	0.410728 - 0.080978 <i>i</i>	0%
0.7	0.418895 - 0.078183 <i>i</i>	0.418895 - 0.078183 <i>i</i>	0.00006%
0.75	0.428728 - 0.073932 <i>i</i>	0.428728 - 0.073932 <i>i</i>	0.00002%
0.769	0.432944 - 0.071693 <i>i</i>	0.432944 - 0.071693 <i>i</i>	0.00003%
$\ell = 2, n = 1$			
0.1	0.347522 - 0.273538 <i>i</i>	0.347687 - 0.273765 <i>i</i>	0.0634%
0.15	0.348714 - 0.273090 <i>i</i>	0.348843 - 0.273259 <i>i</i>	0.0481%
0.2	0.350379 - 0.272452 <i>i</i>	0.350458 - 0.272547 <i>i</i>	0.0278%
0.25	0.352528 - 0.271594 <i>i</i>	0.352561 - 0.271633 <i>i</i>	0.0115%
0.3	0.355189 - 0.270474 <i>i</i>	0.355204 - 0.270495 <i>i</i>	0.0057%
0.35	0.358400 - 0.269057 <i>i</i>	0.358415 - 0.269079 <i>i</i>	0.0058%
0.4	0.362243 - 0.267257 <i>i</i>	0.362250 - 0.267262 <i>i</i>	0.00185%
0.45	0.366756 - 0.264963 <i>i</i>	0.366758 - 0.264960 <i>i</i>	0.0008%
0.5	0.371997 - 0.262057 <i>i</i>	0.372001 - 0.262054 <i>i</i>	0.0011%
0.55	0.378069 - 0.258315 <i>i</i>	0.378070 - 0.258315 <i>i</i>	0.0001%
0.6	0.385043 - 0.253413 <i>i</i>	0.385047 - 0.253419 <i>i</i>	0.0015%
0.65	0.392954 - 0.246806 <i>i</i>	0.392954 - 0.246807 <i>i</i>	$0. \times 10^{-4}$ %
0.7	0.401596 - 0.237556 <i>i</i>	0.401596 - 0.237550 <i>i</i>	0.0013%
0.75	0.409771 - 0.224243 <i>i</i>	0.409772 - 0.224240 <i>i</i>	0.00060%
0.769	0.412108 - 0.217950 <i>i</i>	0.412110 - 0.217947 <i>i</i>	0.00089%
$\ell = 2, n = 2$			
0.1	0.301922 - 0.477390 <i>i</i>	0.303284 - 0.475856 <i>i</i>	0.363%
0.15	0.303648 - 0.476330 <i>i</i>	0.304523 - 0.475374 <i>i</i>	0.229%
0.2	0.306056 - 0.474876 <i>i</i>	0.306558 - 0.474375 <i>i</i>	0.126%
0.25	0.309149 - 0.473015 <i>i</i>	0.309458 - 0.472755 <i>i</i>	0.0715%
0.3	0.312956 - 0.470779 <i>i</i>	0.313473 - 0.470515 <i>i</i>	0.103%
0.35	0.317624 - 0.467931 <i>i</i>	0.317739 - 0.468124 <i>i</i>	0.0397%
0.4	0.323011 - 0.464232 <i>i</i>	0.323026 - 0.464370 <i>i</i>	0.0245%
0.45	0.329187 - 0.459525 <i>i</i>	0.329265 - 0.459916 <i>i</i>	0.0707%
0.5	0.336158 - 0.453558 <i>i</i>	0.329541 - 0.459080 <i>i</i>	1.53%
0.55	0.344078 - 0.445962 <i>i</i>	0.344008 - 0.445701 <i>i</i>	0.0480%
0.6	0.352825 - 0.436132 <i>i</i>	0.352822 - 0.436119 <i>i</i>	0.00236%
0.65	0.361328 - 0.423254 <i>i</i>	0.361950 - 0.423071 <i>i</i>	0.117%
0.7	0.369751 - 0.405120 <i>i</i>	0.369858 - 0.405181 <i>i</i>	0.0225%
0.75	0.372329 - 0.382540 <i>i</i>	0.372319 - 0.382510 <i>i</i>	0.00603%
0.769	0.371221 - 0.373784 <i>i</i>	0.371219 - 0.373930 <i>i</i>	0.0277%

TABLE I. Gravitational quasinormal frequencies for the Bardeen black hole with  $\ell = 2$  and  $M = 1$ , shown as functions of  $\ell_0$  for the fundamental mode ( $n = 0$ ) and the first two overtones ( $n = 1, 2$ ). The second and third columns list the 16th- and 14th-order WKB–Padé values, while the last column gives the percentage difference between the two approximations.

$\ell_0$	WKB16 ( $\tilde{m} = 8$ )	WKB14 ( $\tilde{m} = 7$ )	Difference
$\ell = 3, n = 0$			
0.1	0.600497 - 0.092602 <i>i</i>	0.600497 - 0.092602 <i>i</i>	0%
0.15	0.601828 - 0.092472 <i>i</i>	0.601828 - 0.092472 <i>i</i>	0%
0.2	0.603718 - 0.092284 <i>i</i>	0.603718 - 0.092284 <i>i</i>	0%
0.25	0.606198 - 0.092030 <i>i</i>	0.606198 - 0.092030 <i>i</i>	0%
0.3	0.609306 - 0.091698 <i>i</i>	0.609306 - 0.091698 <i>i</i>	0%
0.35	0.613096 - 0.091275 <i>i</i>	0.613096 - 0.091275 <i>i</i>	0%
0.4	0.617638 - 0.090739 <i>i</i>	0.617638 - 0.090739 <i>i</i>	0%
0.45	0.623026 - 0.090061 <i>i</i>	0.623026 - 0.090061 <i>i</i>	0%
0.5	0.629381 - 0.089197 <i>i</i>	0.629381 - 0.089197 <i>i</i>	0%
0.55	0.636871 - 0.088083 <i>i</i>	0.636871 - 0.088083 <i>i</i>	0%
0.6	0.645725 - 0.086618 <i>i</i>	0.645725 - 0.086618 <i>i</i>	0%
0.65	0.656272 - 0.084631 <i>i</i>	0.656272 - 0.084631 <i>i</i>	0%
0.7	0.669002 - 0.081808 <i>i</i>	0.669002 - 0.081808 <i>i</i>	0%
0.75	0.684670 - 0.077495 <i>i</i>	0.684670 - 0.077495 <i>i</i>	0%
0.769	0.691612 - 0.075187 <i>i</i>	0.691612 - 0.075187 <i>i</i>	0%
$\ell = 3, n = 1$			
0.1	0.583823 - 0.280973 <i>i</i>	0.583823 - 0.280973 <i>i</i>	0%
0.15	0.585311 - 0.280555 <i>i</i>	0.585311 - 0.280555 <i>i</i>	0%
0.2	0.587424 - 0.279950 <i>i</i>	0.587424 - 0.279950 <i>i</i>	0%
0.25	0.590191 - 0.279132 <i>i</i>	0.590191 - 0.279132 <i>i</i>	0%
0.3	0.593654 - 0.278069 <i>i</i>	0.593654 - 0.278069 <i>i</i>	0%
0.35	0.597868 - 0.276713 <i>i</i>	0.597868 - 0.276713 <i>i</i>	0%
0.4	0.602904 - 0.274998 <i>i</i>	0.602904 - 0.274998 <i>i</i>	0%
0.45	0.608853 - 0.272832 <i>i</i>	0.608853 - 0.272832 <i>i</i>	0%
0.5	0.615833 - 0.270079 <i>i</i>	0.615833 - 0.270079 <i>i</i>	0%
0.55	0.623994 - 0.266537 <i>i</i>	0.623994 - 0.266537 <i>i</i>	0.00002%
0.6	0.633524 - 0.261890 <i>i</i>	0.633524 - 0.261890 <i>i</i>	0%
0.65	0.644646 - 0.255614 <i>i</i>	0.644646 - 0.255614 <i>i</i>	0%
0.7	0.657548 - 0.246774 <i>i</i>	0.657548 - 0.246774 <i>i</i>	0%
0.75	0.672003 - 0.233598 <i>i</i>	0.672003 - 0.233598 <i>i</i>	0%
0.769	0.677555 - 0.226871 <i>i</i>	0.677555 - 0.226871 <i>i</i>	0%

TABLE II. Gravitational quasinormal frequencies for the Bardeen black hole with  $\ell = 3$  and  $M = 1$ , shown as functions of  $\ell_0$  for the fundamental mode ( $n = 0$ ) and the first overtone ( $n = 1$ ). The second and third columns list the 16th- and 14th-order WKB–Padé values, while the last column gives the percentage difference between the two approximations.

where  $\omega_0$  is the fundamental quasinormal frequency, and only at later times does it cross over to a power-law tail. Because the far-zone axial potential behaves as in Eq. (28), the usual Price law for asymptotically flat black holes with compact-support initial data applies at fixed radius,

$$\Psi_\ell(t, r) \propto t^{-(2\ell+3)}, \quad t \rightarrow \infty, \quad r = \text{const.} \quad (49)$$

Thus, for the present gravitational mode with  $\ell = 2$ , one expects  $\Psi \propto t^{-7}$ , exactly as seen in the log-log panel of Fig. 2. In this sense the late-time signal follows the standard Price law [96, 120, 121]. The important point is that the quantum-correction parameter changes the quasinormal frequencies appreciably, but it does not change the tail exponent because the large- $r$  structure of the effective potential remains of the Price-law type.

$\ell_0$	WKB16 ( $\tilde{m} = 8$ )	WKB14 ( $\tilde{m} = 7$ )	Difference
$\ell = 3, n = 2$			
0.1	0.553098 - 0.478475 <i>i</i>	0.553099 - 0.478473 <i>i</i>	0.00032%
0.15	0.554881 - 0.477681 <i>i</i>	0.554882 - 0.477680 <i>i</i>	0.00014%
0.2	0.557407 - 0.476531 <i>i</i>	0.557407 - 0.476531 <i>i</i>	0%
0.25	0.560709 - 0.474983 <i>i</i>	0.560709 - 0.474983 <i>i</i>	0.00006%
0.3	0.564830 - 0.472976 <i>i</i>	0.564829 - 0.472975 <i>i</i>	0.00009%
0.35	0.569824 - 0.470424 <i>i</i>	0.569824 - 0.470423 <i>i</i>	0.00010%
0.4	0.575762 - 0.467209 <i>i</i>	0.575762 - 0.467208 <i>i</i>	0.00009%
0.45	0.582728 - 0.463162 <i>i</i>	0.582728 - 0.463162 <i>i</i>	0.00007%
0.5	0.590821 - 0.458042 <i>i</i>	0.590821 - 0.458041 <i>i</i>	0.00009%
0.55	0.600148 - 0.451486 <i>i</i>	0.600149 - 0.451486 <i>i</i>	0.00017%
0.6	0.610797 - 0.442935 <i>i</i>	0.610797 - 0.442935 <i>i</i>	0%
0.65	0.622736 - 0.431480 <i>i</i>	0.622737 - 0.431480 <i>i</i>	0.00008%
0.7	0.635472 - 0.415600 <i>i</i>	0.635473 - 0.415600 <i>i</i>	0.00005%
0.75	0.646798 - 0.393129 <i>i</i>	0.646798 - 0.393128 <i>i</i>	0.00004%
0.769	0.649593 - 0.382667 <i>i</i>	0.649593 - 0.382666 <i>i</i>	0.00003%
$\ell = 3, n = 3$			
0.1	0.513672 - 0.689321 <i>i</i>	0.513679 - 0.689307 <i>i</i>	0.00181%
0.15	0.515827 - 0.688013 <i>i</i>	0.515832 - 0.688006 <i>i</i>	0.00088%
0.2	0.518878 - 0.686124 <i>i</i>	0.518880 - 0.686122 <i>i</i>	0.00038%
0.25	0.522853 - 0.683588 <i>i</i>	0.522852 - 0.683589 <i>i</i>	0.00016%
0.3	0.527797 - 0.680313 <i>i</i>	0.527792 - 0.680314 <i>i</i>	0.00049%
0.35	0.533758 - 0.676166 <i>i</i>	0.533755 - 0.676167 <i>i</i>	0.00039%
0.4	0.540798 - 0.670966 <i>i</i>	0.540795 - 0.670966 <i>i</i>	0.00039%
0.45	0.548982 - 0.664455 <i>i</i>	0.548975 - 0.664454 <i>i</i>	0.00083%
0.5	0.558367 - 0.656262 <i>i</i>	0.558359 - 0.656253 <i>i</i>	0.00142%
0.55	0.568971 - 0.645840 <i>i</i>	0.568979 - 0.645836 <i>i</i>	0.00108%
0.6	0.580690 - 0.632341 <i>i</i>	0.580685 - 0.632342 <i>i</i>	0.00056%
0.65	0.593023 - 0.614459 <i>i</i>	0.593024 - 0.614453 <i>i</i>	0.00069%
0.7	0.604255 - 0.590244 <i>i</i>	0.604256 - 0.590242 <i>i</i>	0.00027%
0.75	0.609422 - 0.558724 <i>i</i>	0.609355 - 0.558799 <i>i</i>	0.0121%
0.769	0.608341 - 0.545838 <i>i</i>	0.608340 - 0.545837 <i>i</i>	0.00002%

TABLE III. Gravitational quasinormal frequencies for the Bardeen black hole with  $\ell = 3$  and  $M = 1$ , shown as functions of  $\ell_0$  for the second and third overtones ( $n = 2, 3$ ). The second and third columns list the 16th- and 14th-order WKB-Padé values, while the last column gives the percentage difference between the two approximations.

## VII. GREY-BODY FACTORS

Grey-body factors describe the frequency-dependent transmission of waves through the curvature-induced potential barrier surrounding the black hole. For the axial gravitational perturbations considered here, one studies the same master equation (22), but now with real frequency  $\Omega > 0$  and with scattering boundary conditions rather than QNM boundary conditions. Choosing a unit-amplitude wave incident from spatial infinity, the asymptotic behavior is

$$\Psi \sim \begin{cases} T_\ell(\Omega)e^{-i\Omega r_*}, & r_* \rightarrow -\infty, \\ e^{-i\Omega r_*} + R_\ell(\Omega)e^{+i\Omega r_*}, & r_* \rightarrow +\infty, \end{cases} \quad (50)$$

where  $R_\ell(\Omega)$  and  $T_\ell(\Omega)$  are the reflection and transmission amplitudes. Since the background is static and the

$\ell$	WKB16 ( $\tilde{m} = 8$ )	WKB14 ( $\tilde{m} = 7$ )	Difference
2	0.432944 - 0.071693 <i>i</i>	0.432944 - 0.071693 <i>i</i>	0.00003%
3	0.691612 - 0.075187 <i>i</i>	0.691612 - 0.075187 <i>i</i>	0%
4	0.931790 - 0.076402 <i>i</i>	0.931790 - 0.076402 <i>i</i>	0%
5	1.164521 - 0.076967 <i>i</i>	1.164521 - 0.076967 <i>i</i>	0%
6	1.393465 - 0.077276 <i>i</i>	1.393465 - 0.077276 <i>i</i>	0%
7	1.620206 - 0.077465 <i>i</i>	1.620206 - 0.077465 <i>i</i>	0%
8	1.845549 - 0.077589 <i>i</i>	1.845549 - 0.077589 <i>i</i>	0%
9	2.069948 - 0.077675 <i>i</i>	2.069948 - 0.077675 <i>i</i>	0%
10	2.293678 - 0.077737 <i>i</i>	2.293678 - 0.077737 <i>i</i>	0%
11	2.516916 - 0.077783 <i>i</i>	2.516916 - 0.077783 <i>i</i>	0%
12	2.739783 - 0.077819 <i>i</i>	2.739783 - 0.077819 <i>i</i>	0%
13	2.962363 - 0.077846 <i>i</i>	2.962363 - 0.077846 <i>i</i>	0%
14	3.184714 - 0.077868 <i>i</i>	3.184714 - 0.077868 <i>i</i>	0%
15	3.406883 - 0.077886 <i>i</i>	3.406883 - 0.077886 <i>i</i>	0%
16	3.628902 - 0.077901 <i>i</i>	3.628902 - 0.077901 <i>i</i>	0%
17	3.850796 - 0.077913 <i>i</i>	3.850796 - 0.077913 <i>i</i>	0%
18	4.072588 - 0.077924 <i>i</i>	4.072588 - 0.077924 <i>i</i>	0%
19	4.294292 - 0.077932 <i>i</i>	4.294292 - 0.077932 <i>i</i>	0%
20	4.515921 - 0.077940 <i>i</i>	4.515921 - 0.077940 <i>i</i>	0%

TABLE IV. Fundamental gravitational quasinormal frequencies ( $n = 0$ ) for the Bardeen black hole with  $M = 1$  and fixed  $\ell_0 = 0.769$ , shown as functions of the multipole number  $\ell$ . The second and third columns list the 16th- and 14th-order WKB-Padé values, while the last column gives the percentage difference between the two approximations.

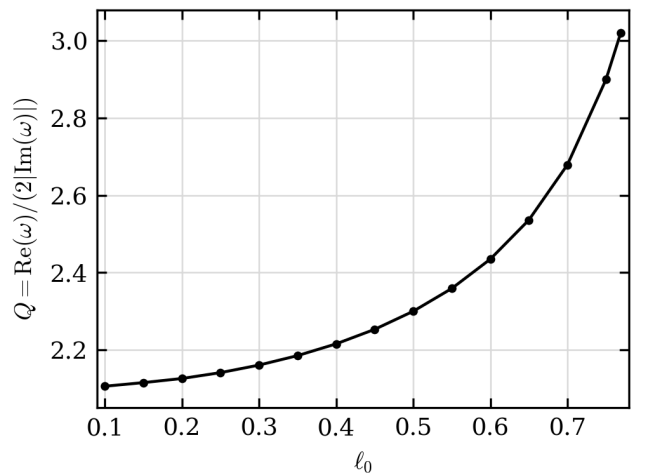


FIG. 3. Quality factor  $Q = \text{Re}(\omega)/(2|\text{Im}(\omega)|)$  for the fundamental axial gravitational mode with  $\ell = 2$ , computed from the WKB16 data in Table I. The monotonic increase with  $\ell_0$  shows that the quantum-corrected Bardeen black hole becomes a progressively better oscillator as one approaches the extremal regime.

effective potential is real, the Wronskian is conserved and one has the standard flux relation

$$|R_\ell(\Omega)|^2 + |T_\ell(\Omega)|^2 = 1. \quad (51)$$

The GBF is therefore defined as

$$\Gamma_\ell(\Omega) \equiv |T_\ell(\Omega)|^2, \quad (52)$$

which measures the fraction of a given partial wave that penetrates the potential barrier. In the scattering picture it is the transmission probability from infinity to the horizon, while in the Hawking-radiation picture the same quantity determines how much of the near-horizon flux reaches an asymptotic observer [10, 64, 122]. Thus, low frequencies are strongly suppressed by the barrier, whereas when  $\Omega^2 \gg V_{\text{ax}}^{\text{max}}$  the barrier becomes nearly transparent and  $\Gamma_\ell(\Omega) \rightarrow 1$ .

Because the effective potential (26) is a smooth, single-peaked barrier, the WKB formalism used for the QNM problem can be applied to the scattering problem as well. At the lowest WKB order, the transmission probability is approximated by the familiar barrier-penetration formula

$$\Gamma_\ell(\Omega) \approx \left[ 1 + \exp\left(\frac{2\pi(V_0 - \Omega^2)}{\sqrt{-2V_2}}\right) \right]^{-1}, \quad (53)$$

where  $V_0 \equiv V_{\text{ax}}(r_0)$  is the value of the potential at its peak and  $V_2 \equiv d^2V_{\text{ax}}/dr_*^2|_{r_*^0} < 0$ . Higher-order corrections are incorporated by the same local expansion around the peak that leads to Eq. (31). Following the WKB treatment of the scattering problem, one introduces a continuous quantity  $\mathcal{K}(\Omega)$  and writes the transmission probability as

$$\Gamma_\ell(\Omega) = \frac{1}{1 + e^{2\pi i\mathcal{K}(\Omega)}}. \quad (54)$$

Here  $\mathcal{K}(\Omega)$  is built from the derivatives of the potential at its maximum exactly in the same way as in the

WKB analysis of quasinormal modes [66, 123]. Unlike in our QNM calculation, we do not use Padé resummation here. Instead, to make the GBF–QNM correspondence explicit, we use the asymptotic formulas derived in Refs. [123, 124] and specialize them to the present static notation.

The basic point is that the same WKB quantity  $\mathcal{K}$  governs both the scattering problem and the resonance problem. In scattering,  $\mathcal{K}(\Omega)$  varies continuously with the real frequency and enters Eq. (54); in the QNM problem, the WKB condition requires  $\mathcal{K} = n + \frac{1}{2}$ , with  $n = 0, 1, 2, \dots$  the overtone number. Thus the fundamental mode  $\omega_0$  and the first overtone  $\omega_1$  encode the same local information about the peak of the potential barrier that determines the GBF. For asymptotically flat black holes and large multipole number  $\ell$ , the correspondence can be written in a particularly compact form. At leading eikonal order one has

$$i\mathcal{K}(\Omega) = \frac{\Omega^2 - \text{Re}(\omega_0)^2}{4\text{Re}(\omega_0)\text{Im}(\omega_0)} + \mathcal{O}(\ell^{-1}), \quad (55)$$

which shows that, once inserted into Eq. (54), the GBF is determined by the real and imaginary parts of the fundamental quasinormal frequency alone. In particular, the transition region between almost complete reflection and almost complete transmission is centered near  $\Omega^2 \simeq \text{Re}(\omega_0)^2$ , while its width is controlled by the damping rate  $|\text{Im}(\omega_0)|$ .

A more accurate relation, including the second-order correction beyond the eikonal limit, reads

$$\begin{aligned} i\mathcal{K}(\Omega) = & \frac{\Omega^2 - \text{Re}(\omega_0)^2}{4\text{Re}(\omega_0)\text{Im}(\omega_0)} \left( 1 + \frac{(\text{Re}(\omega_0) - \text{Re}(\omega_1))^2}{32\text{Im}(\omega_0)^2} - \frac{3\text{Im}(\omega_0) - \text{Im}(\omega_1)}{24\text{Im}(\omega_0)} \right) - \frac{\text{Re}(\omega_0) - \text{Re}(\omega_1)}{16\text{Im}(\omega_0)} \\ & - \frac{(\Omega^2 - \text{Re}(\omega_0)^2)^2}{16\text{Re}(\omega_0)^3\text{Im}(\omega_0)} \left( 1 + \frac{\text{Re}(\omega_0)(\text{Re}(\omega_0) - \text{Re}(\omega_1))}{4\text{Im}(\omega_0)^2} \right) \\ & + \frac{(\Omega^2 - \text{Re}(\omega_0)^2)^3}{32\text{Re}(\omega_0)^5\text{Im}(\omega_0)} \left( 1 + \frac{\text{Re}(\omega_0)(\text{Re}(\omega_0) - \text{Re}(\omega_1))}{4\text{Im}(\omega_0)^2} \right) \\ & + \text{Re}(\omega_0)^2 \left[ \frac{(\text{Re}(\omega_0) - \text{Re}(\omega_1))^2}{16\text{Im}(\omega_0)^4} - \frac{3\text{Im}(\omega_0) - \text{Im}(\omega_1)}{12\text{Im}(\omega_0)} \right] + \mathcal{O}(\ell^{-3}). \end{aligned} \quad (56)$$

Equation (56) makes the correspondence more explicit: beyond the leading barrier-top approximation, the shape of the transmission curve depends not only on the fundamental mode but also on the separation between the fundamental mode and the first overtone. Since the present Bardeen spacetime is static and has no superradiant sector, these non-superradiant correspondence formulas apply directly to each axial gravitational multipole considered here.

The relation between QNMs and GBFs has been investigated extensively in a number of recent works [125–

134], where it was found to provide a reasonably accurate description even for relatively low multipole numbers  $\ell$ . The validity of this correspondence hinges on the same conditions that underlie the applicability of the WKB approximation, in particular the existence of a single, well-defined potential barrier. When this condition is violated such as in the case of a double-well structure of the effective potential [135], or when higher-curvature corrections significantly alter the centrifugal term and lead to instabilities of the background [136–140] the correspondence is expected to break down.

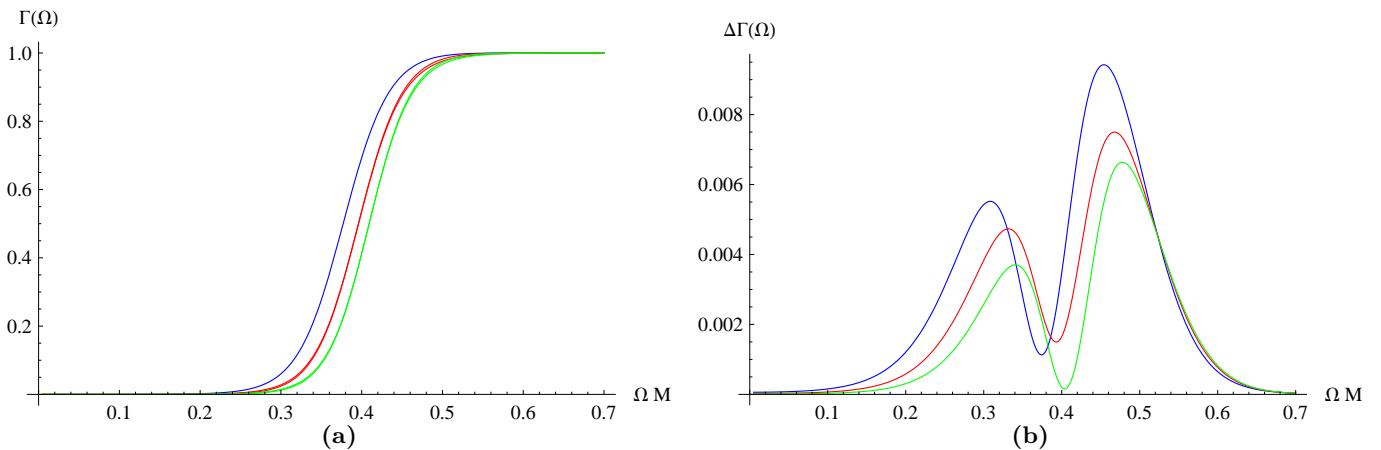


FIG. 4. Comparison of the GBFs for axial gravitational perturbations of the quantum-corrected Bardeen black hole with  $\ell = 2$  and  $M = 1$ . Panel (a) shows the transmission probabilities obtained from the sixth-order WKB method and from the QNM-correspondence formulas for  $\ell_0 = 0.01$  (blue),  $\ell_0 = 0.5$  (red), and  $\ell_0 = 0.769$  (green). Panel (b) shows the absolute difference between the two methods for the same parameter values.

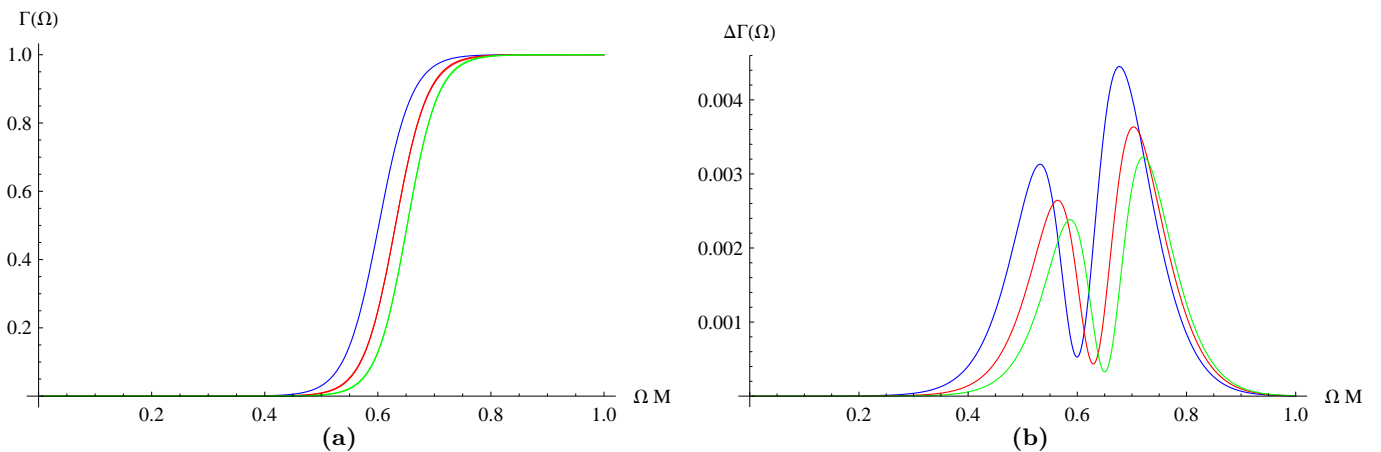


FIG. 5. Comparison of the GBFs for axial gravitational perturbations of the quantum-corrected Bardeen black hole with  $\ell = 3$  and  $M = 1$ . Panel (a) shows the transmission probabilities obtained from the sixth-order WKB method and from the QNM-correspondence formulas for  $\ell_0 = 0.01$  (blue),  $\ell_0 = 0.5$  (red), and  $\ell_0 = 0.769$  (green). Panel (b) shows the absolute difference between the two methods for the same parameter values.

For the representative axial mode  $\ell = 2$  with  $M = 1$ , Fig. 4 compares the GBFs obtained from the sixth-order WKB method with those reconstructed from the QNM correspondence for  $\ell_0 = 0.01$ , 0.5, and 0.769. The same figure also shows the absolute difference between the two approaches.

For the representative axial mode  $\ell = 3$  with  $M = 1$ , Fig. 5 shows the corresponding comparison between the sixth-order WKB GBFs and the QNM-correspondence reconstruction for  $\ell_0 = 0.01$ , 0.5, and 0.769. As before, we also display the absolute difference between the two methods.

Figure 1 provides a direct interpretation of Figs. 4 and 5. Because both increasing  $\ell$  and increasing  $\ell_0$  raise the characteristic barrier height, the condition  $\Omega^2 \sim V_{\text{ax}}^{\text{max}}$  is reached only at larger frequencies. Consequently, the transmission curves shift to the right as  $\ell_0$  increases, and

the  $\ell = 3$  channels turn on later than the  $\ell = 2$  channels. The same barrier ordering explains the stronger suppression of the low-frequency GBFs in the more strongly quantum-corrected cases.

The error plots admit the same interpretation. The absolute differences between the sixth-order WKB result and the QNM-correspondence reconstruction are concentrated in the intermediate-frequency window where the barrier changes from mostly reflective to mostly transparent, while they become negligible in the limits  $\Gamma_\ell \approx 0$  and  $\Gamma_\ell \approx 1$ , where both methods are forced to agree. Moreover, the smaller discrepancies for  $\ell = 3$  are consistent with the more eikonal character of the higher-multipole barrier, for which the local barrier-top information encoded in  $\omega_0$  and  $\omega_1$  reconstructs the transmission curve more accurately.

For  $M = 1$ , Fig. 6 shows the partial and total absorp-

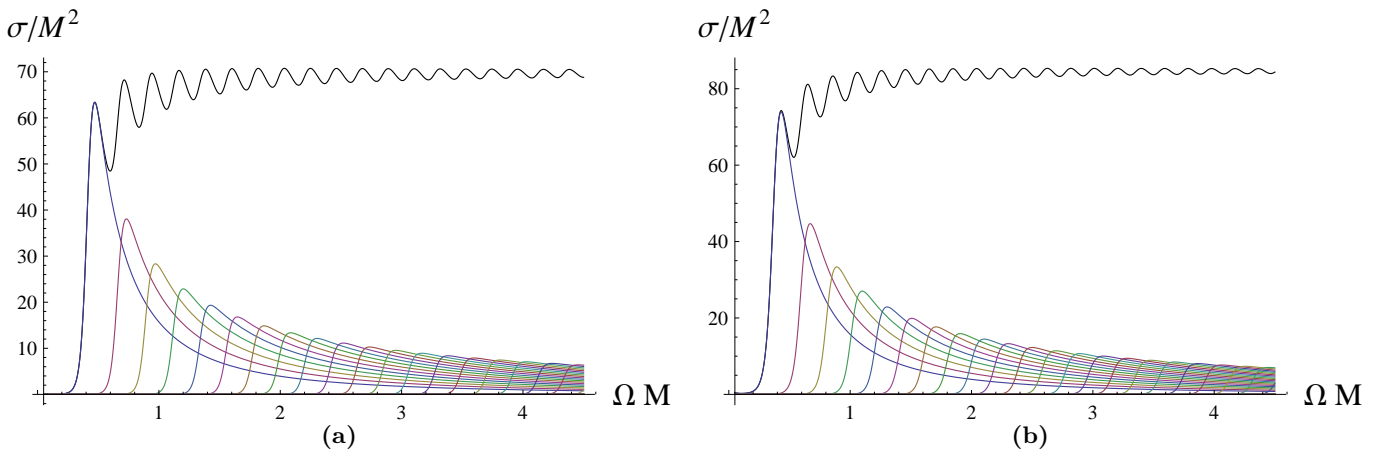


FIG. 6. Partial and total ACSs for axial gravitational perturbations of the quantum-corrected Bardeen black hole with  $M = 1$ . Panel (a) corresponds to  $\ell_0 = 0.01$ , while panel (b) corresponds to  $\ell_0 = 0.769$ . In each panel, the black curve represents the total absorption cross-section and the colored curves represent the partial ACSs of the individual multipoles.

tion cross-sections for the quantum-corrected Bardeen black hole in the two cases  $\ell_0 = 0.01$  and  $\ell_0 = 0.769$ .

The same barrier picture also clarifies Fig. 6. Each colored curve corresponds to a fixed partial wave, and its maximum occurs when the corresponding mode changes from strong reflection to efficient transmission through the barrier. Because the centrifugal part of Eq. (26) makes the barrier higher for larger multipole number, the partial absorption peaks are ordered from left to right as successive  $\ell$  values begin to contribute. The upward shift of the representative barriers in Fig. 1 likewise explains why the partial-wave peaks move to larger  $\Omega M$  when  $\ell_0$  increases from 0.01 to 0.769.

The total cross-section is the sum over these partial contributions, so its oscillatory pattern reflects the successive opening of higher multipoles. In particular, the larger overall level of the  $\ell_0 = 0.769$  curve over the displayed frequency range is consistent with the stronger partial-wave contributions of the more quantum-corrected geometry once the incident frequency becomes large enough to overcome the barrier. In this sense, the ACS data and the GBF data tell the same story: the quantum-correction parameter primarily reorganizes the scattering problem by reshaping the effective potential barrier.

## VIII. CONCLUSIONS

In this work we have studied axial gravitational perturbations of the asymptotically flat Bardeen spacetime in its string-T-duality-inspired quantum-corrected interpretation. Starting from the nonvacuum anisotropic-fluid form of the background, we derived the Regge–Wheeler-type master equation and obtained the compact effective potential (26). The resulting potential is a smooth single barrier that vanishes at the event horizon, reduces to the standard Regge–Wheeler potential in the Schwarzschild

limit, and becomes both higher and more inward-shifted as the quantum-correction parameter  $\ell_0$  increases. This barrier deformation provides the common physical mechanism behind the QNM, GBF, and ACS results obtained in the paper.

Using high-order WKB–Padé techniques, supplemented by time-domain integration and Prony extraction, we found that increasing  $\ell_0$  systematically increases the oscillation frequencies and decreases the damping rates of the axial gravitational modes. In other words, the quantum-corrected Bardeen black hole rings faster and for a longer time than its near-Schwarzschild counterpart, and the quality factor of the fundamental mode grows monotonically toward the near-extremal regime. At fixed  $\ell_0$ , the real part of the fundamental frequency grows almost linearly with the multipole number, whereas the imaginary part approaches an approximately constant eikonal value. The agreement between the 16th- and 14th-order WKB–Padé approximants is excellent for the dominant modes, and the time-domain profile confirms the semianalytic result for the representative  $\ell = 2$  configuration. At late times, the signal still obeys the standard Price-law decay, showing that the near-horizon quantum correction modifies the ringing spectrum much more strongly than the asymptotic tail exponent.

The scattering observables reveal a closely related pattern. Because the effective barrier becomes higher for larger  $\ell$  and larger  $\ell_0$ , the onset of transmission is shifted to higher frequencies and the low-frequency GBFs are more strongly suppressed. The QNM-correspondence formulas reproduce the sixth-order WKB transmission curves rather well, with the best agreement in the regimes of almost complete reflection or transmission and, as expected, even better performance for the more eikonal  $\ell = 3$  case. The partial and total ACSs exhibit the same barrier-governed structure: successive partial-wave peaks appear as higher multipoles begin to penetrate the barrier, while the total cross-section inherits the resulting

oscillatory pattern. Overall, the results indicate that the quantum-correction parameter leaves a coherent imprint on both ringdown and scattering observables, making the Bardeen geometry a useful phenomenological proxy for exploring how short-distance regularization may influence gravitational spectroscopy and black-hole absorption.

#### ACKNOWLEDGMENTS

B. C. L. is grateful to the Excellence project FoS UHK 2205/2025-2026 for the financial support.

#### CONFLICT OF INTEREST

The authors declare no conflict of interest.

#### DATA AVAILABILITY

No data was used for the research described in the article.

- 
- [1] B. P. Abbott *et al.* (LIGO Scientific Collaboration and Virgo Collaboration), *Phys. Rev. Lett.* **116**, 061102 (2016).
- [2] K. D. Kokkotas and B. G. Schmidt, *Living Rev. Relativ.* **2**, 2 (1999).
- [3] E. Berti, V. Cardoso, and A. O. Starinets, *Class. Quantum Grav.* **26**, 163001 (2009).
- [4] S. V. Bolokhov and M. Skvortsova, *Grav. Cosmol.* **31**, 423 (2025), arXiv:2504.05014 [gr-qc].
- [5] R. A. Konoplya and A. Zhidenko, *JHEAp* **44**, 419 (2024), arXiv:2209.00679 [gr-qc].
- [6] P. Kanti and J. March-Russell, *Phys. Rev. D* **66**, 024023 (2002), arXiv:hep-ph/0203223.
- [7] D. N. Page, *Phys. Rev. D* **13**, 198 (1976).
- [8] D. N. Page, *Phys. Rev. D* **14**, 3260 (1976).
- [9] S. W. Hawking, *Commun. Math. Phys.* **43**, 199 (1975).
- [10] R. A. Konoplya, D. Ovchinnikov, and B. Ahmedov, *Phys. Rev. D* **108**, 104054 (2023), arXiv:2307.10801 [gr-qc].
- [11] M. Skvortsova, *Eur. Phys. J. C* **85**, 854 (2025), arXiv:2411.06007 [gr-qc].
- [12] B. C. Lützföglu, *Eur. Phys. J. C* **86**, 39 (2026).
- [13] J. M. Bardeen, in *Proceedings of the 5th International Conference on Gravitation and the Theory of Relativity* (Tbilisi, USSR, 1968) p. 174.
- [14] E. Ayón-Beato and A. García, *Phys. Rev. Lett.* **80**, 5056 (1998).
- [15] E. Ayón-Beato and A. García, *Phys. Lett. B* **493**, 149 (2000).
- [16] B. Toshmatov, Z. Stuchlík, and B. Ahmedov, *Phys. Rev. D* **98**, 085021 (2018), arXiv:1810.06383 [gr-qc].
- [17] B. Toshmatov, Z. Stuchlík, B. Ahmedov, and D. Malafarina, *Phys. Rev. D* **99**, 064043 (2019), arXiv:1903.03778 [gr-qc].
- [18] A. Rincón and V. Santos, *Eur. Phys. J. C* **80**, 910 (2020).
- [19] S. Dey and S. Chakrabarti, *Eur. Phys. J. C* **79**, 504 (2019).
- [20] Y. Zhao, W. Liu, C. Zhang, X. Fang, and J. Jing, *Chin. Phys. C* **48**, 035102 (2024).
- [21] R. A. Konoplya, *JCAP* **07**, 001 (2023), arXiv:2305.09187 [gr-qc].
- [22] K. Lin, J. Li, and S. Yang, *Int. J. Theor. Phys.* **52**, 3771 (2013).
- [23] Y. Yang, D. Liu, Z. Xu, Y. Xing, S. Wu, and Z.-W. Long, *Phys. Rev. D* **104**, 104021 (2021), arXiv:2107.06554 [gr-qc].
- [24] R. A. Konoplya, A. F. Zinhailo, J. Kunz, Z. Stuchlík, and A. Zhidenko, *JCAP* **10**, 091 (2022), arXiv:2206.14714 [gr-qc].
- [25] A. Al-Badawi and A. Kraishan, *Chin. J. Phys.* **87**, 59 (2024).
- [26] O. Pedraza, L. A. López, R. Arceo, and I. Cabrera-Munguia, *Mod. Phys. Lett. A* **37**, 2250057 (2022), arXiv:2111.06488 [gr-qc].
- [27] Y. Guo, H. Xie, and Y.-G. Miao, *Phys. Lett. B* **855**, 138801 (2024), arXiv:2402.10406 [gr-qc].
- [28] E. U. Saka, (2025), arXiv:2512.08904 [gr-qc].
- [29] R. A. Konoplya and A. Zhidenko, *Phys. Rev. D* **113**, 043011 (2026), arXiv:2511.03066 [gr-qc].
- [30] A. Held, R. Gold, and A. Eichhorn, *JCAP* **06**, 029 (2019), arXiv:1904.07133 [gr-qc].
- [31] D. Mahdavian Yekta, M. Karimabadi, and S. A. Alavi, *Annals Phys.* **434**, 168603 (2021), arXiv:1912.12017 [hep-th].
- [32] A. Flachi and J. P. S. Lemos, *Phys. Rev. D* **87**, 024034 (2013), arXiv:1211.6212 [gr-qc].
- [33] M. Skvortsova, (2026), arXiv:2603.28415 [gr-qc].
- [34] X.-C. Cai and Y.-G. Miao, *Phys. Rev. D* **103**, 124050 (2021), arXiv:2104.09725 [gr-qc].
- [35] A. Jawad, M. Yasir, and S. Rani, *Mod. Phys. Lett. A* **35**, 2050298 (2020).
- [36] R. A. Konoplya, Z. Stuchlík, A. Zhidenko, and A. F. Zinhailo, *Phys. Rev. D* **107**, 104050 (2023), arXiv:2303.01987 [gr-qc].
- [37] K. Jusufi, M. Azreg-Ainou, M. Jamil, S.-W. Wei, Q. Wu, and A. Wang, *Phys. Rev. D* **103**, 024013 (2021), arXiv:2008.08450 [gr-qc].
- [38] D. Zhang, H. Gong, G. Fu, J.-P. Wu, and Q. Pan, *Eur. Phys. J. C* **84**, 564 (2024), arXiv:2402.15085 [gr-qc].
- [39] S. Fernando and J. Correa, *Phys. Rev. D* **86**, 064039 (2012), arXiv:1208.5442 [gr-qc].
- [40] L. A. López and V. Ramírez, *Eur. Phys. J. Plus* **138**, 120 (2023), arXiv:2205.10166 [gr-qc].
- [41] P. Dutta Roy and S. Kar, *Phys. Rev. D* **106**, 044028 (2022), arXiv:2206.04505 [gr-qc].
- [42] R. A. Konoplya, D. Ovchinnikov, and B. Ahmedov, *Phys. Rev. D* **108**, 104054 (2023), arXiv:2307.10801 [gr-qc].

- [43] S. V. Bolokhov, *Phys. Rev. D* **109**, 064017 (2024).
- [44] B.-H. Huang, H.-W. Hu, and L. Zhao, *JCAP* **03**, 053 (2024), arXiv:2311.12286 [gr-qc].
- [45] J. Li, K. Lin, and N. Yang, *Eur. Phys. J. C* **75**, 131 (2015), arXiv:1409.5988 [gr-qc].
- [46] S. Mukohyama, K. Takahashi, K. Tomikawa, and V. Yingcharoenrat, *JCAP* **07**, 050 (2023), arXiv:2304.14304 [gr-qc].
- [47] D. M. Gingrich, *Phys. Rev. D* **110**, 084045 (2024), arXiv:2404.04447 [gr-qc].
- [48] R. A. Konoplya, *Phys. Lett. B* **876**, 140386 (2026), arXiv:2603.03189 [gr-qc].
- [49] M. Skvortsova, (2025), arXiv:2509.18061 [gr-qc].
- [50] S. V. Bolokhov, *Annals Phys.* **488**, 170416 (2026), arXiv:2511.12859 [gr-qc].
- [51] A. Dubinsky, *Int. J. Grav. Theor. Phys.* **2**, 6 (2026), arXiv:2603.17644 [gr-qc].
- [52] B. Toshmatov, C. Bambi, B. Ahmedov, Z. Stuchlík, and J. Schee, *Phys. Rev. D* **96**, 064028 (2017), arXiv:1705.03654 [gr-qc].
- [53] Z. Asghar, M. F. Shamir, F. Mofarreh, J. Rayimbaev, O. Sirajiddin, and F. Shayimov, *Nucl. Phys. B* **1025**, 117417 (2026).
- [54] B. Rahmatov, S. Murodov, J. Rayimbaev, Y. Turaev, I. Egamberdiev, K. Badalov, S. Ahmedov, and S. Usanov, *Annals Phys.* **488**, 170366 (2026).
- [55] P. Nicolini, E. Spallucci, and M. F. Wondrak, *Phys. Lett. B* **797**, 134888 (2019), arXiv:1902.11242 [gr-qc].
- [56] S. V. Bolokhov, *Phys. Rev. D* **109**, 064017 (2024).
- [57] M. Saleh, B. B. Thomas, and T. C. Kofané, *Eur. Phys. J. C* **78**, 325 (2018).
- [58] R. A. Konoplya and O. S. Stashko, *Phys. Rev. D* **111**, 104055 (2025), arXiv:2408.02578 [gr-qc].
- [59] B. C. Lütfüoğlu, E. U. Saka, A. Shermatov, J. Rayimbaev, I. Ibragimov, and S. Muminov, *Eur. Phys. J. C* **85**, 1190 (2025), arXiv:2509.15923 [gr-qc].
- [60] Q.-L. Shi, R. Wang, W. Xiong, and P.-C. Li, *Eur. Phys. J. C* **86**, 334 (2026), arXiv:2506.16217 [gr-qc].
- [61] T. Padmanabhan, *Phys. Rev. D* **57**, 6206 (1998).
- [62] S. Chakraborty, G. Compere, and L. Mached, *Phys. Rev. D* **112**, 024015 (2025), arXiv:2412.14831 [gr-qc].
- [63] T. Regge and J. A. Wheeler, *Phys. Rev.* **108**, 1063 (1957).
- [64] P. Boonserm, T. Ngampitipan, and M. Visser, *Phys. Rev. D* **88**, 041502 (2013), arXiv:1305.1416 [gr-qc].
- [65] B. F. Schutz and C. M. Will, *Astrophys. J. Lett.* **291**, L33 (1985).
- [66] S. Iyer and C. M. Will, *Phys. Rev. D* **35**, 3621 (1987).
- [67] R. A. Konoplya, *Phys. Rev. D* **68**, 024018 (2003), arXiv:gr-qc/0303052 [gr-qc].
- [68] J. Matyjasek and M. Opala, *Phys. Rev. D* **96**, 024011 (2017).
- [69] R. A. Konoplya, *Gen. Rel. Grav.* **34**, 329 (2002), arXiv:gr-qc/0109096.
- [70] S. V. Bolokhov and M. Skvortsova, *Eur. Phys. J. C* **86**, 374 (2026), arXiv:2508.19989 [gr-qc].
- [71] D. S. Eniceicu and M. Reece, *Phys. Rev. D* **102**, 044015 (2020), arXiv:1912.05553 [gr-qc].
- [72] R. A. Konoplya and A. F. Zinhailo, *Phys. Rev. D* **99**, 104060 (2019), arXiv:1904.05341 [gr-qc].
- [73] R. Karmakar and U. D. Goswami, *Phys. Scripta* **99**, 055003 (2024), arXiv:2310.18594 [gr-qc].
- [74] R. A. Konoplya and A. Zhidenko, *Phys. Lett. B* **648**, 236 (2007), arXiv:hep-th/0611226.
- [75] Z. Malik, *Int. J. Grav. Theor. Phys.* **2**, 3 (2026), arXiv:2603.18887 [gr-qc].
- [76] B. C. Lütfüoğlu, *Eur. Phys. J. C* **85**, 630 (2025), arXiv:2504.18482 [gr-qc].
- [77] N. Bretón, T. Clark, and S. Fernando, *Int. J. Mod. Phys. D* **26**, 1750112 (2017), arXiv:1703.10070 [gr-qc].
- [78] Y. Guo and Y.-G. Miao, *Phys. Rev. D* **102**, 064049 (2020), arXiv:2005.07524 [hep-th].
- [79] R. A. Konoplya and A. Zhidenko, *Phys. Lett. B* **686**, 199 (2010), arXiv:0909.2138 [hep-th].
- [80] S. V. Bolokhov and M. Skvortsova, *Int. J. Grav. Theor. Phys.* **1**, 3 (2025), arXiv:2507.07196 [gr-qc].
- [81] H. Ishihara, M. Kimura, R. A. Konoplya, K. Murata, J. Soda, and A. Zhidenko, *Phys. Rev. D* **77**, 084019 (2008), arXiv:0802.0655 [hep-th].
- [82] P. Wongjun, C.-H. Chen, and R. Nakarachinda, *Phys. Rev. D* **101**, 124033 (2020), arXiv:1910.05908 [gr-qc].
- [83] R. A. Konoplya and A. Zhidenko, *Phys. Rev. D* **82**, 084003 (2010), arXiv:1004.3772 [hep-th].
- [84] M. Skvortsova, *Eur. Phys. J. C* **85**, 854 (2025), arXiv:2411.06007 [gr-qc].
- [85] S. Fernando, *Gen. Rel. Grav.* **48**, 24 (2016), arXiv:1601.06407 [gr-qc].
- [86] A. Pathrikar, *Int. J. Grav. Theor. Phys.* **1**, 1 (2026), arXiv:2510.01376 [gr-qc].
- [87] R. A. Konoplya, *Phys. Lett. B* **784**, 43 (2018), arXiv:1805.04718 [gr-qc].
- [88] M. Momennia, S. Hossein Hendi, and F. Soltani Bidgoli, *Phys. Lett. B* **813**, 136028 (2021), arXiv:1807.01792 [hep-th].
- [89] R. A. Konoplya and E. Abdalla, *Phys. Rev. D* **71**, 084015 (2005), arXiv:hep-th/0503029.
- [90] S. V. Bolokhov, K. A. Bronnikov, and M. V. Skvortsova, *Int. J. Grav. Theor. Phys.* **2**, 2 (2026), arXiv:2507.14603 [gr-qc].
- [91] E. Abdalla, R. A. Konoplya, and C. Molina, *Phys. Rev. D* **72**, 084006 (2005), arXiv:hep-th/0507100.
- [92] K. D. Kokkotas, R. A. Konoplya, and A. Zhidenko, *Phys. Rev. D* **83**, 024031 (2011), arXiv:1011.1843 [gr-qc].
- [93] Z. Malik, *Int. J. Grav. Theor. Phys.* **1**, 6 (2025), arXiv:2509.15995 [gr-qc].
- [94] M. Skvortsova, *EPL* **149**, 59001 (2025), arXiv:2503.03650 [gr-qc].
- [95] Y. Sekhmani, S. K. Murya, J. Rayimbaev, M. Altanji, I. Ibragimov, and S. Muminov, *Nucl. Phys. B* **1023**, 117311 (2026).
- [96] C. Gundlach, R. H. Price, and J. Pullin, *Phys. Rev. D* **49**, 883 (1994), arXiv:gr-qc/9307009 [gr-qc].
- [97] G. R. de Prony, *Journal de l'École Polytechnique* **1**, 24 (1795).
- [98] R. A. Konoplya and A. Zhidenko, *Phys. Lett. B* **853**, 138685 (2024), arXiv:2307.01110 [gr-qc].
- [99] M. Skvortsova, *Grav. Cosmol.* **30**, 279 (2024), arXiv:2405.15807 [gr-qc].
- [100] M. Skvortsova, *Grav. Cosmol.* **30**, 68 (2024), arXiv:2311.02729 [gr-qc].
- [101] S. V. Bolokhov, *Eur. Phys. J. C* **84**, 634 (2024), arXiv:2404.09364 [gr-qc].
- [102] Z. Malik, *Annals Phys.* **479**, 170046 (2025), arXiv:2409.01561 [gr-qc].
- [103] N. Varghese and V. C. Kuriakose, *Gen. Rel. Grav.* **43**, 2757 (2011), arXiv:1011.6608 [gr-qc].

- [104] S. V. Bolokhov, *Phys. Lett. B* **856**, 138879 (2024), arXiv:2310.12326 [gr-qc].
- [105] R. A. Konoplya and A. Zhidenko, *Phys. Rev. D* **89**, 024011 (2014), arXiv:1309.7667 [hep-th].
- [106] B. C. Lütfüoğlu, *Eur. Phys. J. C* **85**, 486 (2025), arXiv:2503.16087 [gr-qc].
- [107] M. Skvortsova, *Fortsch. Phys.* **72**, 2400036 (2024), arXiv:2311.11650 [gr-qc].
- [108] J. P. Arbelaez, (2026), arXiv:2601.22340 [gr-qc].
- [109] E. Abdalla, O. P. F. Piedra, F. S. Nuñez, and J. de Oliveira, *Phys. Rev. D* **88**, 064035 (2013), arXiv:1211.3390 [gr-qc].
- [110] M. Skvortsova, *Fortsch. Phys.* **72**, 2400132 (2024), arXiv:2405.06390 [gr-qc].
- [111] B. Hamil, A. Al-Badawi, and B. C. Lütfüoğlu, *Phys. Scripta* **100**, 105008 (2025), arXiv:2505.18611 [gr-qc].
- [112] Z. Malik, *Int. J. Theor. Phys.* **63**, 199 (2024), arXiv:2308.10412 [gr-qc].
- [113] S. V. Bolokhov, (2026), arXiv:2603.22310 [gr-qc].
- [114] J. P. Arbelaez, (2025), arXiv:2509.25141 [gr-qc].
- [115] A. Dubinsky, *Int. J. Grav. Theor. Phys.* **1**, 2 (2025), arXiv:2507.00256 [gr-qc].
- [116] R. A. Konoplya and A. Zhidenko, *Phys. Rev. D* **109**, 104005 (2024), arXiv:2403.07848 [gr-qc].
- [117] S. V. Bolokhov, *Phys. Rev. D* **110**, 024010 (2024), arXiv:2311.05503 [gr-qc].
- [118] A. Dubinsky and A. F. Zinhailo, *EPL* **149**, 69004 (2025), arXiv:2410.15232 [gr-qc].
- [119] S. V. Bolokhov, (2026), arXiv:2604.11845 [gr-qc].
- [120] R. A. Konoplya and A. Zhidenko, *Rev. Mod. Phys.* **83**, 793 (2011), arXiv:1102.4014 [gr-qc].
- [121] R. H. Price, *Phys. Rev. D* **5**, 2419 (1972).
- [122] D. N. Page, *Phys. Rev. D* **13**, 198 (1976).
- [123] R. A. Konoplya and A. Zhidenko, *JCAP* **09**, 068 (2024), arXiv:2406.11694 [gr-qc].
- [124] R. A. Konoplya and A. Zhidenko, *Phys. Lett. B* **861**, 139288 (2025), arXiv:2408.11162 [gr-qc].
- [125] Z. Malik, (2025), arXiv:2510.06689 [gr-qc].
- [126] B. C. Lütfüoğlu, A. Shermatov, J. Rayimbaev, M. Matyoqubov, and O. Sirajiddin, *Eur. Phys. J. C* **85**, 1484 (2025), arXiv:2511.22366 [gr-qc].
- [127] B. C. Lütfüoğlu, (2026), arXiv:2603.24424 [gr-qc].
- [128] S. V. Bolokhov and M. Skvortsova, *JCAP* **04**, 025 (2025), arXiv:2412.11166 [gr-qc].
- [129] B. C. Lütfüoğlu, *Phys. Lett. B* **872**, 140082 (2026), arXiv:2510.25969 [gr-qc].
- [130] A. Dubinsky, *Mod. Phys. Lett. A* **40**, 2550111 (2025), arXiv:2412.00625 [gr-qc].
- [131] B. C. Lütfüoğlu, J. Rayimbaev, S. Murodov, J. Kurbanov, and M. Matyoqubov, (2026), arXiv:2604.14999 [gr-qc].
- [132] Z. Malik, (2024), arXiv:2412.13385 [gr-qc].
- [133] B. C. Lütfüoğlu, *Int. J. Grav. Theor. Phys.* **1**, 4 (2025), arXiv:2507.09246 [gr-qc].
- [134] B. C. Lütfüoğlu, *Fortsch. Phys.* **74**, e70074 (2026), arXiv:2510.10579 [gr-qc].
- [135] R. A. Konoplya and O. S. Stashko, *Phys. Rev. D* **111**, 084031 (2025), arXiv:2502.05689 [gr-qc].
- [136] R. A. Konoplya and A. Zhidenko, *Phys. Rev. D* **95**, 104005 (2017), arXiv:1701.01652 [hep-th].
- [137] R. A. Konoplya and A. Zhidenko, *JCAP* **05**, 050 (2017), arXiv:1705.01656 [hep-th].
- [138] G. Dotti and R. J. Gleiser, *Class. Quant. Grav.* **22**, L1 (2005), arXiv:gr-qc/0409005.
- [139] T. Takahashi and J. Soda, *Prog. Theor. Phys.* **124**, 711 (2010), arXiv:1008.1618 [gr-qc].
- [140] R. A. Konoplya and A. Zhidenko, *JHEP* **09**, 139 (2017), arXiv:1705.07732 [hep-th].